BB

INS Report

INS-Rep.-1142
May 1996

Single and Double Delta Production in the $^3He(\gamma,\pi^+\pi^-)$ Reaction at 380 MeV $\leq E_\gamma \leq$ 700 MeV

D.G. Watts[a], G.M. Huber*, G.J. Lolos
Department of Physics, University of Regina, Regina, SK S4S 0A2 Canada

B. Lasiuk[b]
Department of Physics, University of Saskatchewan, Saskatoon, SK S7N 0W0 Canada

S. Kato, M. Koike, K. Maruyama, K. Niki
Institute for Nuclear Study, University of Tokyo, Tanashi, Tokyo 188, Japan

Y. Wada
Meiji College of Pharmacy, Setagaya, Tokyo 154, Japan

K. Maeda, T. Suda
Department of Physics, Tohoku University, Sendai 980, Japan

T. Emura, H. Miyamoto
Department of Applied Physics, Tokyo University of Agriculture and Technology, Koganei, Tokyo 184, Japan

S. Endo, Y. Sumi
Department of Physics, Hiroshima University, Higashi-Hiroshima 724, Japan

O. Konno, H. Yamazaki
Laboratory of Nuclear Science, Tohoku University, Sendai 982, Japan

H. Itoh
Department of Physics, Saga University, Saga 840, Japan

T. Maki
University of Occupational and Environmental Health, Kitakyushu 807, Japan

A. Sasaki
College of General Education, Akita University, Akita 010, Japan

(The TAGX Collaboration)

Institute for Nuclear Study
University of Tokyo
Tanashi, Tokyo 188, Japan

(Submitted to Phys. Rev. C)

Single and Double Delta Production in the ^{3}He$(\gamma, \pi^+\pi^-)$ Reaction at 380 MeV $\leq E_\gamma \leq$ 700 MeV

D.G. Watts[a], G.M. Huber*, G.J. Lolos
Department of Physics, University of Regina, Regina, SK S4S 0A2 Canada

B. Lasiuk[b]
Department of Physics, University of Saskatchewan, Saskatoon, SK S7N 0W0 Canada

S. Kato, M. Koike, K. Maruyama, K. Niki
Institute for Nuclear Study, University of Tokyo, Tanashi, Tokyo 188, Japan

Y. Wada
Meiji College of Pharmacy, Setagaya, Tokyo 154, Japan

K. Maeda, T. Suda
Department of Physics, Tohoku University, Sendai 980, Japan

T. Emura, H. Miyamoto
Department of Applied Physics, Tokyo University of Agriculture and Technology, Koganei, Tokyo 184, Japan

S. Endo, Y. Sumi
Department of Physics, Hiroshima University, Higashi-Hiroshima 724, Japan

O. Konno, H. Yamazaki
Laboratory of Nuclear Science, Tohoku University, Sendai 982, Japan

H. Itoh
Department of Physics, Saga University, Saga 840, Japan

T. Maki
University of Occupational and Environmental Health, Kitakyushu 807, Japan

A. Sasaki
College of General Education, Akita University, Akita 010, Japan

(The TAGX Collaboration)
(April 22, 1996)

Results are presented for the $^3He(\gamma, \pi^+\pi^-)$ reaction in the region 380 $MeV \leq E_\gamma \leq$ 700 MeV, investigated with the use of a 10% duty factor tagged photon beam, in conjunction with the TAGX multiparticle spectrometer. The study of such multipion photoproduction reactions is a test of chiral symmetric models, and is expected to provide an insight on the role of the Δ and N^* resonances in the nuclear medium. From comparisons of the data with simple reaction simulations, it was found that the data were best fit with a combination of multibody phase space channels, quasifree Δ and N^*, and $\Delta\Delta$ production channels. The results are compared with other double pion photoproduction reactions on hydrogen and deuterium.

13.60.Le,25.20.Lj,25.20.-x

*Corresponding Author: FAX: 306-585-4894, E-mail: huberg@meena.cc.uregina.ca

I. INTRODUCTION

For photon energies above 550 MeV, the cross section of multipion production on a proton target exceeds that of single pion photoproduction, and rapidly rises to account for nearly all of the $\gamma p \rightarrow Hadrons$ cross section in the few GeV region. Thus, an understanding of multipion photoproduction reactions is crucial to understanding the photon-nucleus interaction in this energy region. Several multipion photoproduction experiments were carried out in the 1970's using bubble chamber techniques, and the findings are summarized in the review

article by Luke and Soding [1]. Briefly, it was found that the $\gamma p \rightarrow \Delta^{++}\pi^-$ process dominates the region below ρ meson energies, and has a strong, real, nonresonant $J^\pi = 3/2^-$ partial wave near threshold, from the contact interaction, in addition to pion exchange and s channel resonance contributions. The ratio of the cross section of this process to the $\gamma p \rightarrow \Delta^o\pi^+$ reaction was measured below 700 MeV (9:1) and is consistent with $I = 1/2$ in the s channel, or isovector t channel exchange.

In recent years, a related reaction, pion-induced pion production $(\pi, 2\pi)$ has received intense scrutiny [2–6] due to advances in the treatment of chiral symmetric Lagrangians [7]. These models are formulated as the low-energy limit of QCD, incorporating a chiral symmetric Lagrangian, with the physical chiral symmetry breaking treated as a perturbation. This introduces new nonlinear (loop) terms into the expressions for the pion-nucleon couplings, which do not occur in nuclear theories based on isospin symmetry alone.

The chiral symmetric framework has recently been applied to the problem of double pion photoproduction at threshold by Dahm [8], and recently expanded by Benmerrouche and Tomusiak [9] to include Δ contributions. These calculations, using a chirally symmetric Lagrangian, but without loop or chiral corrections, show promise in determining corrections to the low energy theorem (LET) result. It is hoped that double pion photoproduction experiments on hydrogen and other light nuclei will yield empirical constraints on the nonlinear couplings that lead to these LET corrections.

These expectations also apply to the model created by Gomez-Tejedor and Oset [10] for the $p(\gamma, \pi^+\pi^-)p$ reaction. They found, in comparison to their model for the $p(\pi, \pi^+\pi^-)p$ reaction, that the photoproduction reaction is more heavily dominated by Δ-terms, even at low energies close to threshold, that nonresonant terms have little strength in the reaction, and that the role of N^* intermediate states is much less important at threshold, but becomes more important above 800 MeV, where the $\gamma N \rightarrow N*_{1520} \rightarrow \Delta\pi$ process interferes strongly with the contact interaction (Kroll-Ruderman) term. This model was extended [11] to the $d(\gamma, \pi^+\pi^-p)n$ reaction, and the two-body exchange currents leading to $\Delta\Delta$ production were derived. A natural extension of this work would be to other light nuclei.

Given the revived interest in the field of multipion production, it is fortunate that a new generation of high duty cycle tagged photon beams have made these experiments easier to perform. With the upgrade of the INS electron synchrotron in 1985, tagged photon beams, with a duty factor of 10-20% and energy up to 1.12 GeV, are available. Double pion production data on the deuteron, from this facility, have recently been published [12] for the energy range $570 \leq E_\gamma \leq 850$ MeV. The newly commissioned tagged photon beam facility at Mainz has also yielded proton target results [13] from 450 to 800 MeV.

In this paper, we present, for the first time, results for the $^3He(\gamma, \pi^+\pi^-)$ reaction, which was carried out simultaneously with the previously reported single-pion production experiment [14]. It is hoped that the results presented may inspire models incorporating effective chiral Lagrangians to be extended to the nuclear domain, as well as to assist in the understanding of the short-range contributions to nucleon-nucleon interactions from Δ_{1232} excitation. Section II of this paper discusses the equipment and techniques used in the experiment, while section III discusses the methods of particle identification and event selection used in the data analysis. Section IV presents comparisons of the data with Monte Carlo simulations and cross sections for the modelled reaction channels. Section V summarizes the conclusions of this work.

II. EXPERIMENTAL TECHNIQUE

The TAGX facility has been described in detail elsewhere [15], so only a brief description is given here.

A. Tagged Photon Beam

INS employs a 15 MeV injector linac coupled to a 1.3 GeV electron synchrotron to produce a tagged photon beam with a duty factor of 10-20% [16]. For this experiment, the nominal value of the synchrotron energy, E_S, was 800 MeV, and the duty factor was approximately 10%, which corresponds to an electron beam pulse extraction time of 5 ms. As the energy of the synchrotron, E_S, varies sinusoidally with a 47 ms period, the determination of the instantaneous energy of the extracted electrons, E_e, was determined by measuring the electron extraction timing from the synchrotron with online electronics.

The extracted electrons were then incident upon a thin platinum radiator, which produces bremsstrahlung photons in the vicinity of a rectangular analyzer magnet with field strength of 1.17 T. The scattered electrons were bent out of the beamline by the field, to intersect an array of 32 electron tagging counters and 8 backing counters, which determine the energies of the tagged photons via the difference in electron energies before and after scattering from the radiator, $E_\gamma = E_e - E_{e'}$. Each element in the tagging array had a scattered electron momentum acceptance of 10 MeV/c, yielding a total tagging array coverage from 380 MeV to 700 MeV. The magnet/tagging counter system will be referred to as the tagger in this work. The average tagged photon intensity was kept to 2×10^5 γ/s, to reduce the rate of accidental event triggers.

Due to the collimation of the photon beamline downstream of the tagger, not all of the tagger hits recorded correspond to tagged photons incident upon the target. To correct the number of tagger hits for the number of tagged photons, the tagging efficiency of each of the 32 taggers was found by setting a lead-glass Čerenkov

counter in the photon beam downstream of the target, to measure the ratio of tagged photons to the number of tagger hits. The tagging efficiencies, η_{tag}, of $80 \pm 2\%$, and the radiator in/out ratios of 1 to 2%, were used to correct the tagger count rate to yield the tagged photon rate.

After these corrections, the total number of tagged photons in each energy bin was:

$$N_\gamma(E_\gamma = 420 \pm 40\ MeV) = 37.2 \times 10^9$$
$$N_\gamma(E_\gamma = 500 \pm 40\ MeV) = 41.5 \times 10^9$$
$$N_\gamma(E_\gamma = 580 \pm 40\ MeV) = 47.4 \times 10^9$$
$$N_\gamma(E_\gamma = 660 \pm 40\ MeV) = 56.6 \times 10^9$$

B. Liquid ^{3}He Target

The design and operation of the ^3He target is described in reference [17]. The target cell was connected, via a long, thin, vertical, stainless steel pipe, to the refrigeration system located above the TAGX spectrometer magnet. The target cell was a cylinder of 50 mm diameter and 90 mm height. The target cell's vacuum wall was a honeycomb design of Nomex plastic [18] of 3.3×10^{-3} radiation lengths [19]. The target temperature for the experiment was $1.986 \pm 0.001\ K$, corresponding to a density of $0.0786\ g/cm^3$ for the ^3He.

C. TAGX Spectrometer

The TAGX magnetic spectrometer had a charged particle acceptance of $\pi\ sr$ and a neutral particle acceptance of $0.85\ sr$. Two identical semi-cylindrical drift chambers (CDCs), two sets of counter hodoscopes (IH and OH), and four electromagnetic background (EM) veto counters were located in the magnet gap. A top view of TAGX is shown in figure 1.

1. Analyzer Magnet

The dipole magnet had a 60 cm pole gap and a 107 cm circular pole face diameter, with a nominal field strength of $0.5\ T$. The distribution of the magnetic field was measured at 10^4 points with Hall probes, and the measured nonuniformities were taken into account in the offline data analysis.

2. Cylindrical Drift Chambers (CDCs)

The two CDCs, surrounding the target area, were employed to determine the charged particle momentum via track reconstruction. The CDCs spanned horizontal angles from 15^o to 165^o, on both sides of the beamline, and a vertical acceptance of $\pm 18.3^o$. Each CDC contained 1100 gold-plated molybdenum wires for field shaping, 230 gold-plated tungsten wires for drift-time readout, and 94 stainless steel wires for charge-division readout (not used in this work). The wires were strung vertically and arranged in twelve concentric layers. The sense wires were held at $2.95\ kV$ voltage (the field-shape wires being grounded) and used in a gas mixture of 50% Ar and 50% C_2H_6. Signals from the sense wires were amplified by charge-sensitive preamplifiers and fed into discriminator modules. They were then digitized with standard CAMAC TDCs for the drift-time measurements.

3. Counter Hodoscopes

The two sets of plastic scintillator hodoscopes, inner and outer (IH and OH), were employed to give triggering signals to the online acquisition system, and to measure the time-of-flight (TOF) of charged particles. The IHs consisted of 12 (6×2) 5 mm thick scintillator elements, located inside the inner surface of the CDCs, on a circle of 75 mm radius about the target cell. As the IHs were within the magnetic field region of the analyzer magnet, photomultipliers with fine-mesh dynodes were used.

The OHs consisted of 33 (16+17) 10 mm thick scintillator elements. Each OH was equipped with photomultipliers attached to both vertical ends, to allow determination of the track angle with respect to the median plane of the spectrometer, placed outside of the magnetic field. The TOF resolution measured between the OH and IH was found to be 0.75 ns.

4. Electromagnetic Background Veto Counters

Although the geometry of the spectrometer was such that the system avoided high amounts of electromagnetic background from direct interaction with the photon beam, electron-positron pairs were still swept into the spectrometer by the analyzer magnetic field, possibly mimicking real events. To prevent this, four sets of veto counters were placed horizontally across the front ($\theta < 90^o$) and back ($\theta > 90^o$) OH counters, in the median plane of the spectrometer. Each element consisted of a plastic scintillator 155 mm long, 50 mm high and 5 mm thick. A signal taken from any one of the veto counters was taken to indicate the presence of pair-production accidentals background, and the event was rejected.

D. Trigger and Data Acquisition

The pair-production accidental rate precluded the use of single-arm triggering, and the trigger condition thus required that there be at least one charged particle on

each side of the photon beamline (in each CDC hemisphere). A two-level trigger system was employed to optimize the data taking. A pretrigger consisting of:

$$PT = IH_L \cdot IH_R \cdot \Sigma TAGB \cdot \overline{EMveto_F}$$

(coincidence between the IHs, the back photon taggers, and the absence of the forward EM veto counters) was used as the gate signal for the ADCs and as the start signal for the TDCs. The pretrigger rate was typically $\sim 2\ kHz$. The main trigger consisted of the logical product of the pretrigger with the OH signal, the main tagger signal, the absence of the back EM veto signal, and the absence of the computer inhibit signal;

$$MT = PT \cdot OH_L \cdot OH_R \cdot \Sigma TAG \cdot \overline{EMveto_B} * \overline{Inhibit}.$$

If the main trigger was satisfied within a 400 ns period, the event was recorded, otherwise, the CAMAC modules were cleared, and the system awaited the next trigger. The main trigger rate was $\sim 20\ Hz$. The trigger system is explained in further detail in reference [20].

Three processors were used for the recording and analyzing of events. The event-by-event readout was performed by a microcomputer, with the data stored in CAMAC memory modules of 140 event capacity. These data were stored on tape, and also sent to an analysis computer running in parallel. This analysis provided preliminary analyses, including track reconstruction and particle identification. The acquisition system livetime, η_{live}, was 97.4%.

III. DATA ANALYSIS

This work used the standard TAGX event reconstruction analysis, which has been described in reference [15]. Here, we describe the most important points of the analysis procedure.

A. Background Rejection and Track Reconstruction

To reduce the large amount of pair-production background present in the data sample, cuts were placed on the TDC spectra for each of the 32 taggers, and all events with a simultaneous coincidence between two (or more) tagging counters were rejected. This had the effect of reducing the background by 90%. A sample timing histogram for one tagger before these cuts were applied is shown in figure 2.

The track reconstruction was used as the basis for further event rejection. As the confidence in the track determination decreases with the presence of background, and as the rejection of background depends, in part, on track determination, an iterative process between track determination and background rejection was employed.

For the purpose of the offline analysis, the CDCs were considered to be divided into 15 sections, each subtending 10^o. A track was then considered to be reconstructible if it spaned less than 5 adjacent sections, and each section contained between 4 and 20 sense wire hits (each section contained between 25 and 35 sense wires). All events whose tracks did not conform to these limits were rejected.

A spline-fitting method was employed to reconstruct the particle track. Particle charge, emission angle, and momentum were determined for each individual track, with the momentum resolution being $\Delta p/p = 9 \times 10^{-5}p + 10^{-2}$, where Δp and p are both measured in MeV/c. In determining the particle tracks, the track-fitting routines took into account both the nonuniformities in the TAGX magnetic field, as well the as the asymmetries in ionization drift times, due to the effect of the TAGX magnetic field upon the ions arriving from either the left or the right of a sense wire.

In extrapolating the particle tracks to the target area, it was found that not all event origins intersected the target cell, as determined by the point of closest approach between the tracks for an event. A 'target cut' was imposed on event origins, requiring that they exist within or near the target cell. This had the effect of removing many events due to pair production in the air upstream of the target cell. Initially, a generous 5 cm target cut is used (the target cell being 2.5 cm in diameter), and later a more stringent target cut was used when the confidence in track reconstruction was more certain. Furthermore, 27% of the beam sample was dedicated to empty target cell runs, which were subtracted from the data.

In order to ensure the rejection of the bulk of the pair-production background, two requirements are imposed, that one of the two detected particles has a momentum of 150 MeV/c or greater, and that the other detected particle has a momentum of at least 100 MeV/c (as calculated in the center of the target). This requirement was found to remove the remaining electromagnetic-induced background events.

B. Particle Identification

The momentum, p, obtained from the CDC track fitting, and the time-of-flight, TOF, provided by the OH-IH scintillator timing, give the mass of a particle according to:

$$mc^2 = \frac{p}{c}\sqrt{(\frac{c \times TOF}{d_{path}})^2 - 1},$$

where d_{path} is the distance traveled by the particle between the IH and the OH, taking into account the track curvature in the TAGX magnetic field. This distance varies between 75 and 95 cm for the pions in this experiment.

If the particle mass is between 0 and 400 MeV/c^2, it is tentatively identified as a pion, and energy loss corrections are applied to reconstruct the energy at the cen-

ter of the target. Figure 3 shows the separation in pion identification bands realized at the end of this analysis. The upper band corresponds to π^+ tracks, and the lower band is due to π^- tracks. In order to be identified as a pion, the particle must have momentum between 100 and 500 MeV/c, and must fall in one of the two loci in figure 3. All events in the figure are due to the $\pi^+\pi^-$ coincidences discussed in this work. The lack of extra bands in the figure indicates the successful removal of the data sample's unwanted pair-production background events.

C. Event Reconstruction

The number of $\pi^+\pi^-$ events remaining after the analysis and empty target subtraction was:

$$Y(E_\gamma = 420 \pm 40\ MeV) = 86$$
$$Y(E_\gamma = 500 \pm 40\ MeV) = 722$$
$$Y(E_\gamma = 580 \pm 40\ MeV) = 1659$$
$$Y(E_\gamma = 660 \pm 40\ MeV) = 2161$$

From the reconstructed pion momenta, $\vec{p_1}, \vec{p_2}$, the invariant mass, $\pi^+\pi^-$ opening angle, missing momentum components, missing energy, and missing mass were calculated for each event according to:

$$InvariantMass = \frac{\sqrt{(E_1+E_2)^2 - (\vec{p_1}+\vec{p_2})^2c^2}}{c^2}$$

$$OpeningAngle = ArcCos(\frac{\vec{p_1}\cdot\vec{p_2}}{p_1 p_2})$$

$$MissingMomentum, \vec{p_m} = \vec{p_\gamma} - \vec{p_1} - \vec{p_2}$$

$$MissingEnergy, E_m = E_\gamma - E_1 - E_2$$

$$MissingMass = \frac{\sqrt{E_m^2 - p_m^2c^2}}{c^2}.$$

Monte Carlo simulations, described in the next section, provided the acceptance of the detector system as a function of incident photon energy. Although the acceptance for pions with momenta greater than 100 MeV/c was π sr, the choice of reaction mechanism causes the $\pi^+\pi^-$ coincidence acceptance to differ from the product of the individual particle acceptances because of emission angle correlations, or because the available energy may require that the pions are often emitted below the detection threshold. Typical values of the coincidence acceptance for the reaction mechanisms studied were 0.5% to 0.9%.

Figure 4 indicates a small, expected, left-right asymmetry in the momentum-emission angle correlation of the spectrometer for low momenta π^+ and π^-. This asymmetry is because oppositely charged particles follow paths of differing curvature in the spectrometer magnetic field, resulting in slightly different forward angle acceptances for the two particle types. The asymmetry is mirror symmetric for the two particle types across the beamline, and was incorporated in the acceptance simulations.

IV. SIMULATIONS AND RESULTS

A. Simulations

Several different simulations of possible channels for the $^3He(\gamma, \pi^+\pi^-)$ reaction were performed, all incorporating the full geometry of the spectrometer. Of these channels, those combinations which yielded the most satisfactory fit to the data were selected, and the others were removed from further analysis. Those channels which have been identified in our data are:

1. quasifree Δ production, in which the incident photon is absorbed by one nucleon, simultaneously exciting it to a Δ and emitting a pion; the Δ then decays to produce the second pion. Earlier work [1] shows that $\gamma p \rightarrow \Delta^{++}\pi^-$ is the dominant two pion production process on the proton in this energy range, although $\gamma p \rightarrow \Delta^o\pi^+$ also contributes. The $\gamma n \rightarrow \Delta^-\pi^+$ reaction proceeds with about half of the corresponding proton cross section [21]. The two remaining nucleons in ^3He are spectators. For our simulation, the $\gamma^3He \rightarrow \pi^-\Delta^{++}(pn)_{SP}$ reaction was modelled, and the other channels incorporated via isospin corrections.

2. quasifree N^*_{1440} production, in which the incident photon is absorbed by a neutron, simultaneously exciting it to a N^*_{1440} and emitting a π^-. This resonance then decays into a π^+n. This is the only N^* mechanism that results in a $\pi^+\pi^-$ pair.

3. $\Delta\Delta$ production, in which the photon is absorbed on two nucleons, exciting them to Δs, which then decay to produce two pions. In this case, the reaction $\gamma pn \rightarrow \Delta^{++}\Delta^-$ dominates, although $\gamma pn \rightarrow \Delta^+\Delta^o$ also contributes. The spectator nucleon momentum in all three of these simulations was peaked near 90 MeV/c, in accordance with Fermi-momentum expectations [22].

4. three-body phase space, $\gamma^3He \rightarrow \pi^+\pi^-{}^3He$, in which the recoil nucleus is left intact.

5. five-body phase space, $\gamma^3He \rightarrow \pi^+\pi^-ppn$, in which the recoil nucleus is broken into its three nucleonic components. Four-body phase space was excluded, on the grounds that the resulting particle distributions would be nearly indistinguishable from five-body phase space, considering that the binding energy of the deuteron (and, hence, the difference between four-body and five-body energy constraints) is only 2.22 MeV.

The contributions of each of the modeled reaction channels were determined by their fits to the observed missing mass, missing momentum, $\pi^+\pi^-$ opening angle, and $\pi^+\pi^-$ invariant mass distributions. These fits, for each of the four photon energy bins, are shown in figures 5-8. The agreement between the experimental distributions and the sum of the models fit is generally acceptable, although there are some discrepancies. We find that the experimental invariant mass and missing momentum distributions peak slightly more sharply than the sum of the simulations is able to reproduce, and that the missing mass distribution peaks at a slightly higher value than could be modelled. The opening angle distributions are fit reasonably well, considering the statistical fluctuations in the data. The fits are clearly more successful at describing the data below 540 MeV, than above this energy.

We have investigated several alternate processes, in order to gain more insight into these differences between the data and the simulations.

1. Final state pion-nucleus interactions:
   It has been reported recently [23] that approximately 30% of the $^3He(\pi^+, ppp)$ events were due to the two step process, $\pi N \rightarrow \pi' N'$, followed by $\pi NN \rightarrow NN$ absorption. At the highest energy of this work, the emitted pions have approximately 140 MeV energy, each, which can certainly produce FSI. However, quasielastic $\pi N \rightarrow \pi' N'$ scattering will only remove energy from the detected (scattered) pion, and, thus, the deviation from the simulations in figure 6 will be even more pronounced.

2. Three pion production, $\gamma^3He \rightarrow \pi^+\pi^-\pi^o{}^3He$ and $^3He(\gamma, \eta)X$:
   The detection threshold for the three pion production reaction in our experiment is about $E_\gamma = 520\ MeV$, and the experiment also covers the dynamic range where the $\eta \rightarrow \pi^+\pi^-\pi^o$ is produced. In these cases, the unobserved π^o carries away momentum according to three body phase space, and removes energy equal to or greater than its rest mass. Such processes populate regions of missing momentum, in figure 6, where the simulations already overpredict the data, and does not address the source of the discrepancy.

We are led to conclude that the discrepancies between the sum of the simulation fits and the data are due to no one specific cause, but are probably the cumulative effect of approximations to the ^3He medium in our simple models.

B. Cross Sections

The cross sections for each reaction channel over each energy bin were calculated according to:

$$\sigma(E) = \frac{Y}{N_\gamma \eta_{live} \eta_{det} \rho_{tgt}},$$

where Y is the number of 'fitted' events in a given energy bin, N_γ is the total number of photons incident on the target for that energy bin, η_{live} is the livetime of the computer's acquisition electronics, η_{det} is the detection efficiency of the TAGX spectrometer for the reaction channel in question (given by the Monte Carlo simulation for each reaction channel and energy bin), and ρ_{tgt} is the target density as seen by the incident photon beam (in $nuclei/cm^2$).

The cross sections assigned to each reaction channel, for each energy bin, are listed in table 1. Figures 9-11 show that these cross sections are in line with reasonable expectations. The stated error bars include all sources of statistical and systematic error, of which a very large contribution is due to the uncertainty in the fits presented above.

The cross sections in figure 9 include both the Δ and N^* channels. This is consistent with the presentation of the older $\gamma p \rightarrow \Delta^{++}\pi^-$ results [1], which clearly indicate the presence of N^* resonances in the cross section energy dependence. This is justifiable, because the broad N^*_{1440} ($\Gamma > 250\ MeV$) significantly overlaps the Δ_{1232} resonance. Our cross sections rise rapidly with energy, from threshold to 550 MeV, and then flatten to a value that is below that of three times the analogous Δ excitation cross sections on the proton. This could be due to the fact that the $\gamma n \rightarrow \Delta^-\pi^+$ cross section is smaller than that of the proton. It should also be noted that the cross sections of reference [12], also obtained with the TAGX spectrometer, are for the $d(\gamma, \pi^+\pi^- p)n$ reaction. However, the 300 MeV/c proton detection requirement of that experiment effectively excludes events in which the proton is a spectator. The cross section which they identify as being due to the $\Delta^{++}\pi^- n_{SP}$ process is treated as proton data here.

The $\Delta\Delta$ cross sections, in figure 10, appear to rise with energy, but with some uncertainties. In this case, the neutron must play a role in both the deuteron and ^3He experiments, and the agreement between the two (after multiplication by 1.5) is much better. Our new results make it much clearer that the calculation of Gomez-Tejedor et al. [11] significantly underestimates the strength of this channel at energies very close to the channel threshold. While predictions based on chiral symmetry are expected to be accurate at very small external momenta, there are ongoing questions about the application of chiral loop corrections, even at threshold. The model of Ref. [11] contains several ingredients other than chiral symmetry, and it is likely that one of these other factors is responsible for the failure of their calculation to reproduce the low energy data. A speculation on the cause of this deficiency may be an incomplete treatment of the Γ of the Δ resonances, whose low mass components play an especially important role at threshold.

The near constancy of the sum of the phase space chan-

nels in figure 11 is expected, after noting the constancy of the deuteron's phase space channel with photon energy.

C. Summary and Conclusions

A pioneering study of the $^3He(\gamma,\pi^+\pi^-)$ reaction has been performed with incident photon energies from 380 MeV to 700 MeV, using the TAGX spectrometer. The energy range of this reaction, close to multipion emission threshold, allows the predictions of chiral symmetric models to be tested. It also allows the further investigation into the role of the Δ, and other resonances, in the nuclear medium.

Three of the reaction channels considered were those of quasifree Δ and N^*_{1440}, and $\Delta\Delta$ production, in addition to the usual phase space reaction channels (three and five-body). The cross sections found for these channels have been presented for four incident photon energy ranges, 420 ± 40 MeV, 500 ± 40 MeV, 580 ± 40 MeV, 660 ± 40 MeV. The single delta channel rises with energy up to 550 MeV, and then plateaus at a level less than three times the equivalent cross section on the proton. The double delta channel cross section exceeds the low energy expectations of a recently published model based on a chiral symmetric Lagrangian [11], but this is likely due to other ingredients of the model. Both phase space reactions are relatively constant over the four energy regions.

To extend these results further, multipion photoproduction should be performed on other light nuclei, and at higher energies. Work is currently underway at TAGX to extend the $^3He(\gamma,\pi^+\pi^-)$ reaction to 1120 MeV, and to incorporate the effects of the ρ^0 resonance into the analysis. The study of this, and other reactions, will help extend our knowledge of photon-nucleon interactions.

V. ACKNOWLEDGMENTS

We would like to thank C. Rangacharyulu for his invaluable help with the experiment and data calibration, N. Mobed for helpful discussions, and A. Sakaguchi for the data conversion program. We also would like to acknowledge the support and hospitality of the staff of the INS electron synchrotron and the staff of the computer room at INS.

This analysis was performed with the use of the INS computer and was supported in part by the Grant-in-Aid for Special Project Research on Meson Science of the Ministry of Education, Science and Culture of Japan, the Natural Sciences and Engineering Research Council of Canada, and the Saskatchewan Department of Economic Development.

---

[a] Present Address: Department of Physics, University of Waterloo, Waterloo, ON N2L 3G1 Canada.
[b] Present Address: Department of Physics, University of California, Los Angeles, CA 90024.

[1] D. Luke, P. Soding, Springer Tracts Mod. Phys. **59** (1971) 39.
[2] J. Lichtenstadt, et al., Phys. Rev. C **33** (1986) 655.
[3] M. Sevior, et al., Phys. Rev. Lett. **66** (1991) 2569.
[4] A. Rahav, et al., Phys. Rev. Lett. **66** (1991) 1279.
[5] R. Rui, et al., Nucl. Phys. **A517** (1990) 455.
[6] O. Jakel, et al., Nucl. Phys. **A511** (1990) 733.
[7] J.F. Donoghue, E. Golowich, B.R. Holstein, "Dynamics of the Standard Model", Cambridge Univ. Press, 1992.
S. Weinberg, Phys. Lett. **B295** (1992) 114.
U. von Klock. Phys. Rev. C **49** (1994) 2932.
V. Bernard, N. Kaiser, Ulf-G. Meissner, Int. J. Mod. Phys. **E4** (1995) 193.
[8] R. Dahm, Proc. Seventh Amsterdam Mini-Conf. 'Electromagnetic Production of Mesons on Nucleons and Nuclei', H.P. Blok, J.H. Koch, H. de Vries, eds., NIKHEF-K (1991), 207.
[9] M. Benmerrouche, E. Tomusiak, Phys. Rev. Lett. **73** (1994) 400.
[10] J.A. Gomez-Tejedor, E. Oset, Nucl. Phys. **A571** (1994) 667.
[11] J.A. Gomez-Tejedor, E. Oset, H. Toki, Phys. Lett. **B346** (1995) 240.
[12] M. Asai, et al., Zeit. Phys. **A344** (1993) 335.
[13] A. Braghieri, et al., 'πN Newsletter', D. Drechsel, G. Hohler, W. Kluge, B.M.K. Nefkens, eds., **10** (1995) 141.
[14] T. Emura, et al., Phys. Lett. **B306** (1993) 6.
[15] K. Maruyama et al., Nucl. Instr. Meth. (in press).
[16] K. Yoshida, et al. IEEE Trans. Nucl. Sci. **NS-32** (1985) 2688.
[17] S. Kato, et al., Nucl. Instr. Meth. **A290** (1990) 315.
S. Kato, et al. Nucl. Instr. Meth. **A307** (1991) 213.
[18] Trademark of DuPont Corp., Delaware, USA.
[19] M. Harada, et al., Nucl. Instr. Meth. **A276** (1989) 451.
[20] K. Niki, et al. Nucl. Instr. A **294** (1990) 534.
[21] F. Carbonara, et al., Nuo. Cim. **36** (1976) 219.
[22] E. Jans, et al., Nucl. Phys. **A475** (1987) 687.
[23] G. Backenstoss, et al., Paul Scherrer Institut Preprint, PR-95-27, December, 1995.
[24] ABBHHM (Aachen-Berlin-Bonn-Hamburg-Heidelburg-München) Collaboration, Phys. Rev. **175** (1968) 1669.
[25] G. Gialanella, et al., Nuo. Cim. **63** (1969) 892.

TABLES

Mechanism	E_γ [MeV]	$\sigma \pm \delta\sigma$ [μb]
Phase Space		
	420±40	17±11
	500±40	8±4
	580±40	31±10
	660±40	28±9
Quasifree Δ and N^*		
	420±40	34±20
	500±40	96±31
	580±40	108±33
	660±40	99±30
$\Delta\Delta$		
	500±40	11±4
	580±40	23±7
	660±40	28±8

TABLE I. Reaction channel cross sections and uncertainties for the four photon energy bins. The reported error bars include all statistical and systematic errors, including those of the simulation fitting procedure.

FIGURE CAPTIONS

FIG. 1. The TAGX spectrometer consists of two semi-cylindrical drift chambers (CDC) situated in a 0.5 T magnetic field for momentum determination, two sets (IH and OH) of plastic hodoscopes for time-of-flight determination, and an upstream photon tagging facility. The tagging system was calibrated with the use of the lead-glass Čerenkov detector shown downstream of the spectrometer.

FIG. 2. Sample timing coincidence plot for an element (TAG#15) of the photon tagging array before final data processing.

FIG. 3. Charge × momentum, from the CDC, versus time-of-flight, from the OH-IH scintillator timing, for π^+ and π^- coincidences detected in this experiment. The upper band is due to π^+ tracks, and the lower band is due to π^- tracks. Proton candidates, falling outside to the upper right limit of the plot, are not shown. The lower pion momentum threshold of 100 MeV/c (corrected for energy loss from the center of the target) is clearly visible. Electron/positron tracks are largely confined to the region between -100 and +100 MeV/c in this figure, and the absence of structure along the threshold cut indicates the successful removal of the data sample's unwanted background events.

FIG. 4. Charge × momentum versus horizontal emission angle for π^+ and π^- detected in this experiment. The left-right difference in π^+ and π^- distributions are the result of differing TAGX acceptances for low momentum tracks at forward angles. Positively charged pions curve clockwise in the spectrometer magnetic field (as seen from above) and so have larger acceptance for beam-right emission than beam-left emission. Negatively charged pions curve counter-clockwise, and so have mirror symmetric acceptance.

FIG. 5. Fits for the missing mass over the energy bins a) E_γ = 420±40 MeV, b) E_γ = 500±40 MeV, c) E_γ = 580±40 MeV, d) E_γ = 660±40 MeV. The filled circles correspond to the data, while the solid line is the sum of the quasifree Δ and N^* mechanisms, the dashed line is the $\Delta\Delta$ mechanism, the dotted line is the sum of the three and five-body phase space, and the double thick line is the sum of the simulations.

FIG. 6. Experimental distribution and simulations for the missing Momentum. The legend is the same as in figure 5.

FIG. 7. Experimental distribution and simulations for the $\pi^+\pi^-$ opening angle. The legend is the same as in figure 5.

FIG. 8. Experimental distribution and simulations for the $\pi^+\pi^-$ invariant mass. The legend is the same as in figure 5.

FIG. 9. Cross sections for the sum of Δ and N^* excitation contributions of this work, as described in the text, and previous related works. The plotting symbols are as follows: [solid square] This work, $\gamma^3He \rightarrow \Delta\pi NN_{SP}$. [diamond] Ref. [21], [empty square] Ref. [24], [triangle] Ref. [25], all $\gamma p \rightarrow \Delta^{++}\pi^-$ data, multiplied by three. [solid circle] Ref. [12], $\gamma d \rightarrow \Delta^{++}\pi^- n_{SP}$ data, also multiplied by three, as described in the text.

FIG. 10. Cross sections for the $\Delta\Delta$ excitation contribution of this work, and previous related works. The plotting symbols are as follows: [solid square] This work, $\gamma^3He \rightarrow \Delta\Delta N_{SP}$. [solid circle] Ref. [12], $\gamma d \rightarrow \Delta^{++}\Delta^-$ data, multiplied by 1.5. The curve is the calculation for the $\gamma d \rightarrow \Delta^{++}\Delta^-$ reaction of Ref. [11], multiplied by 1.5.

FIG. 11. Cross sections for the phase space contribution of this work, and previous related works. The plotting symbols are as follows: [solid square] This work, sum of three and five-body phase space on ^3He, as described in the text. [solid circle] Ref. [12], four-body phase space on d multiplied by 1.5.

Fig. 1

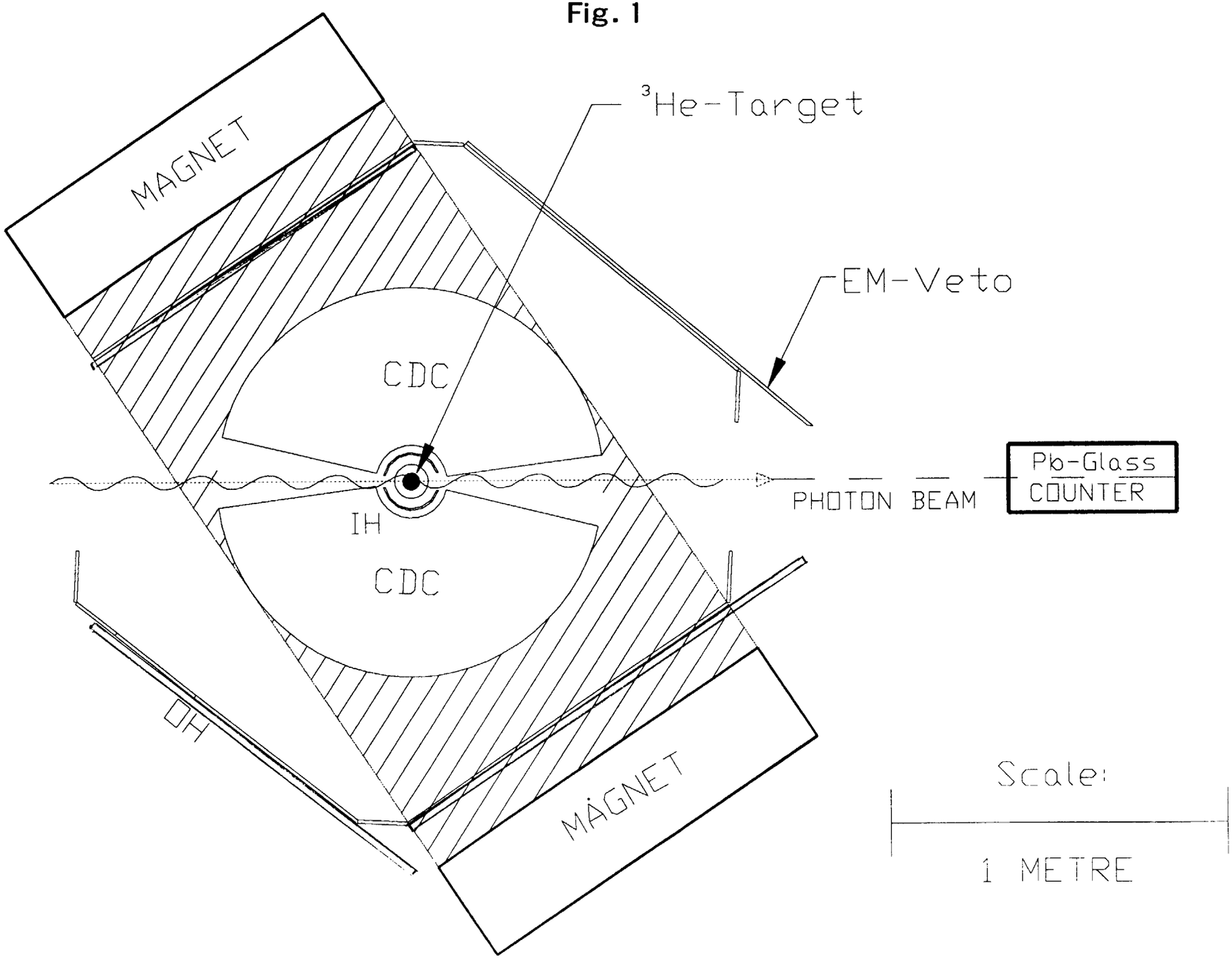
MAGNET
^{3}He-Target
EM-Veto
CDC
IH
CDC
PHOTON BEAM
Pb-Glass
COUNTER
OH
MAGNET
Scale:
1 METRE

Fig. 2

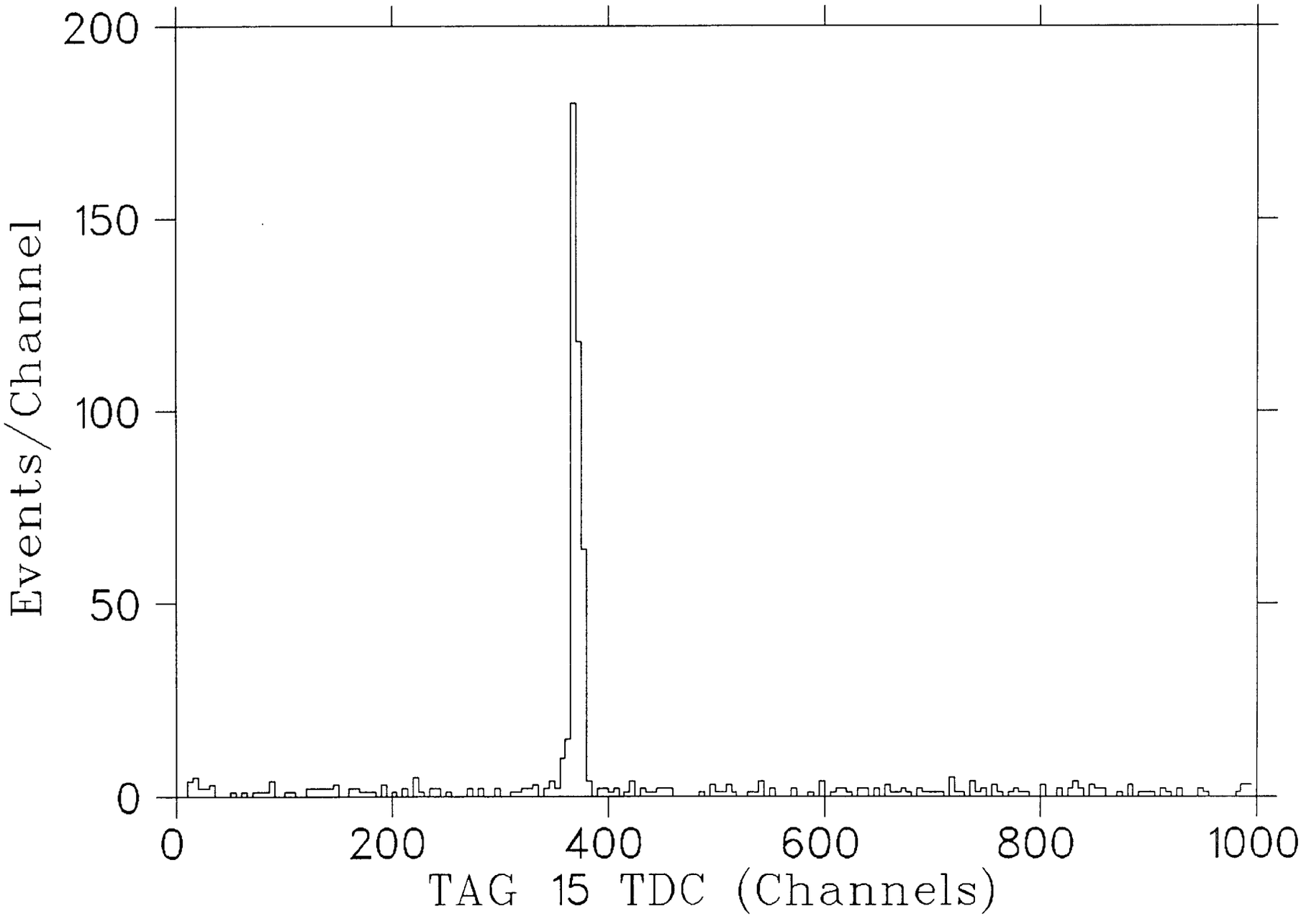
200
150
100
50
0
Events/Channel
0
200
400
600
800
1000
TAG 15 TDC (Channels)

Fig. 3

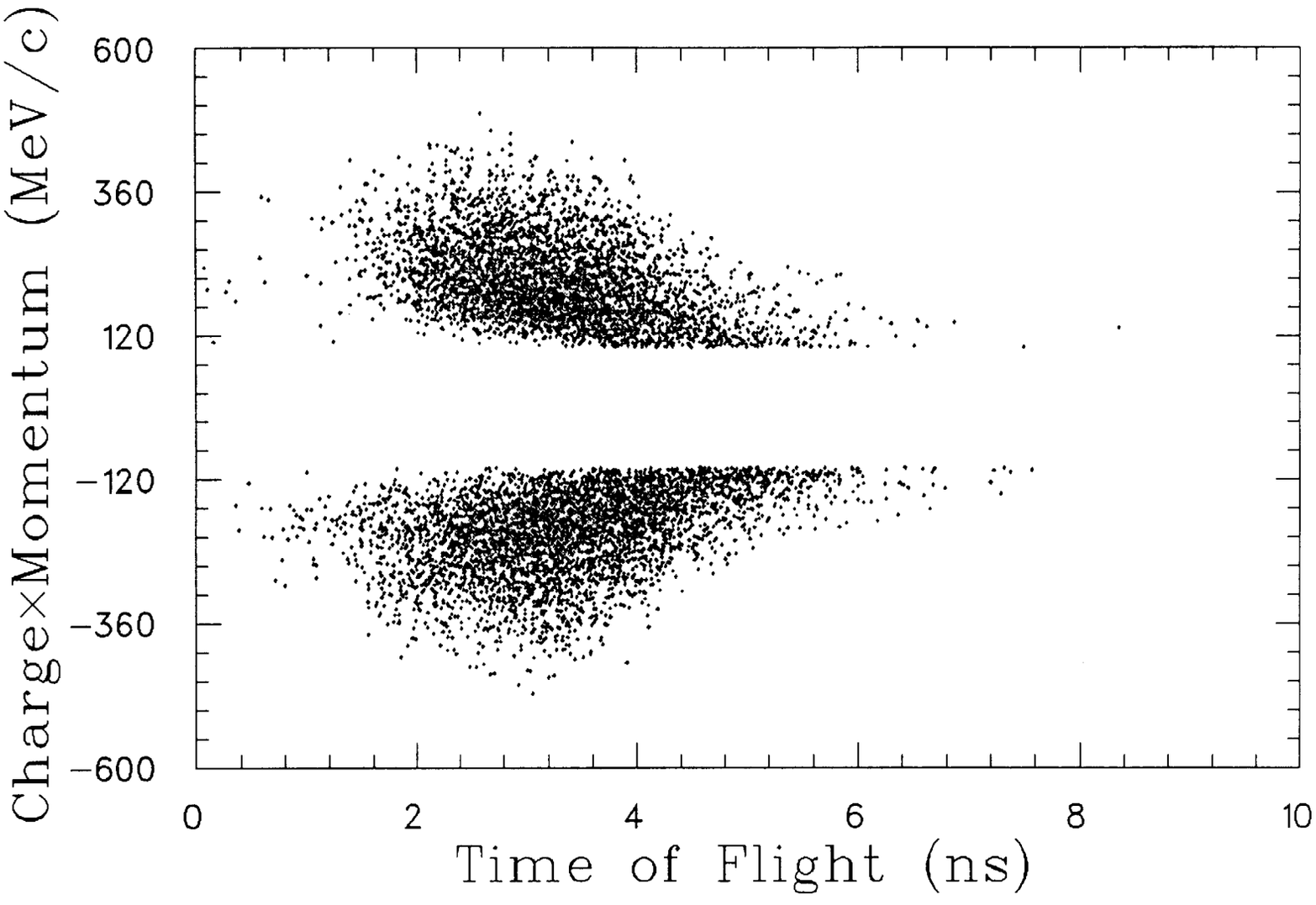
Charge×Momentum (MeV/c)
600
360
120
−120
−360
−600
0
2
4
6
8
10
Time of Flight (ns)

Fig. 4

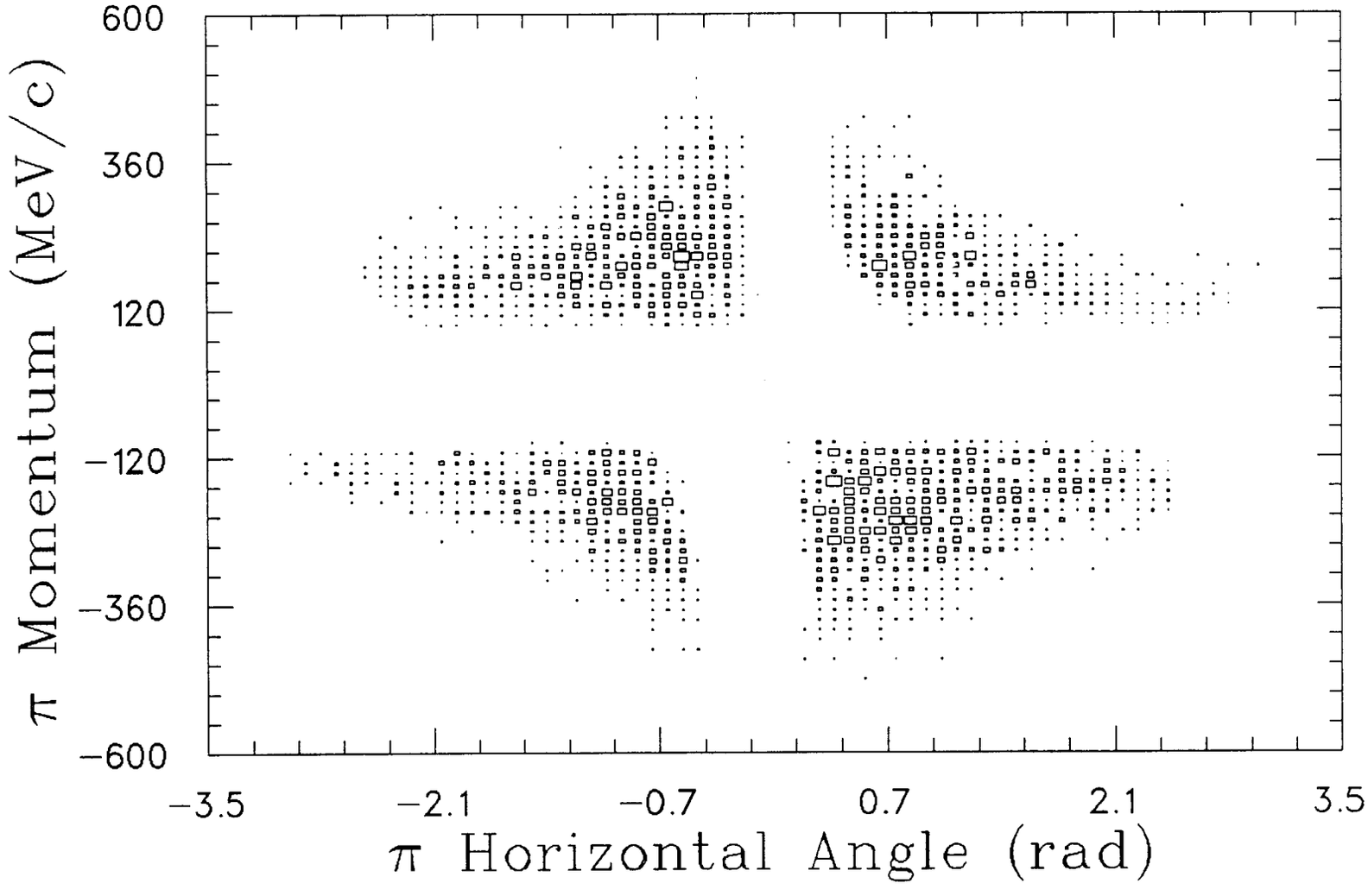
600
360
120
−120
−360
−600
π Momentum (MeV/c)
−3.5
−2.1
−0.7
0.7
2.1
3.5
π Horizontal Angle (rad)

Fig. 5

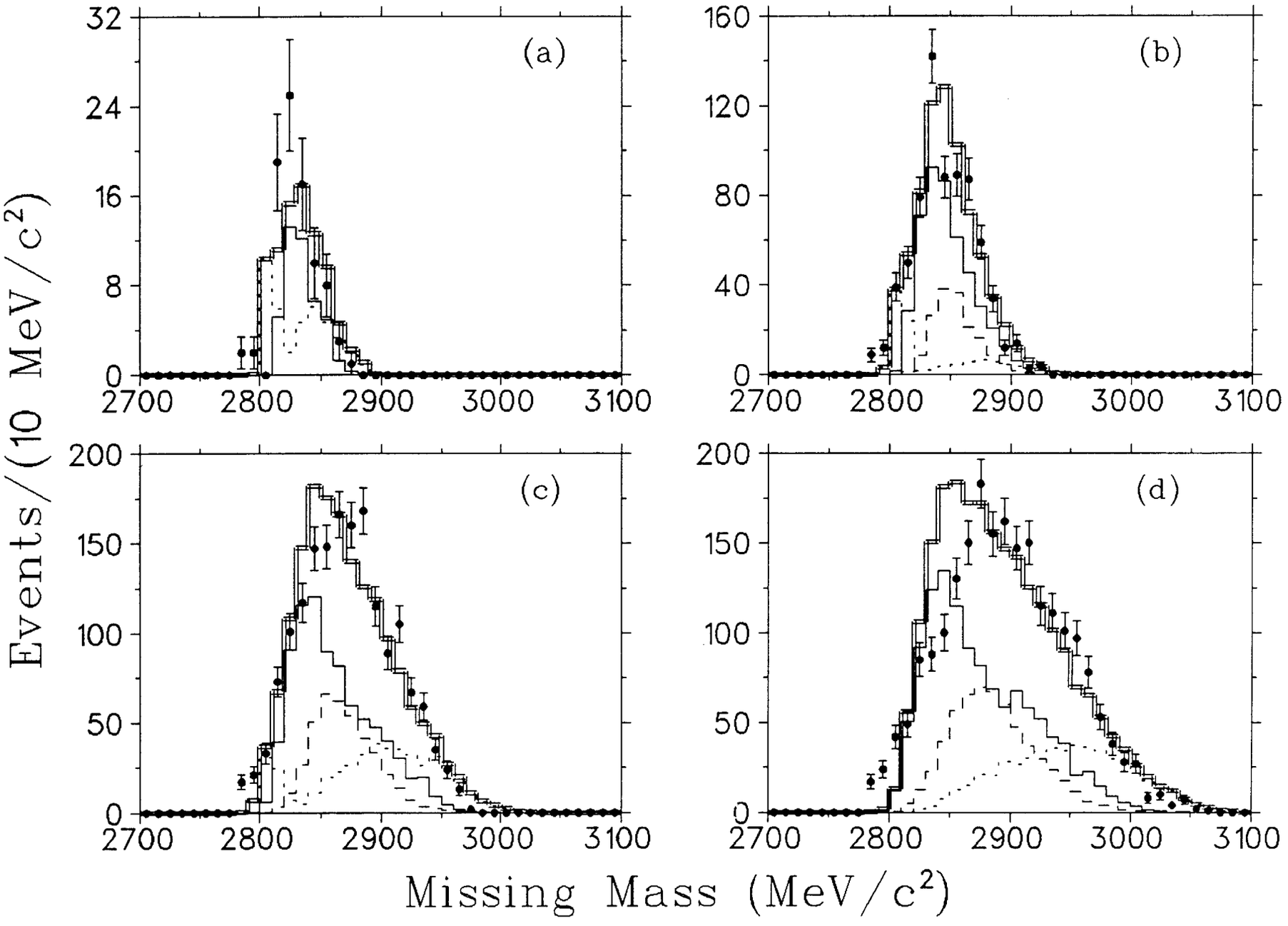
(a)
(b)
(c)
(d)
Events/(10 MeV/c²)
Missing Mass (MeV/c²)
2700
2800
2900
3000
3100

Fig. 6

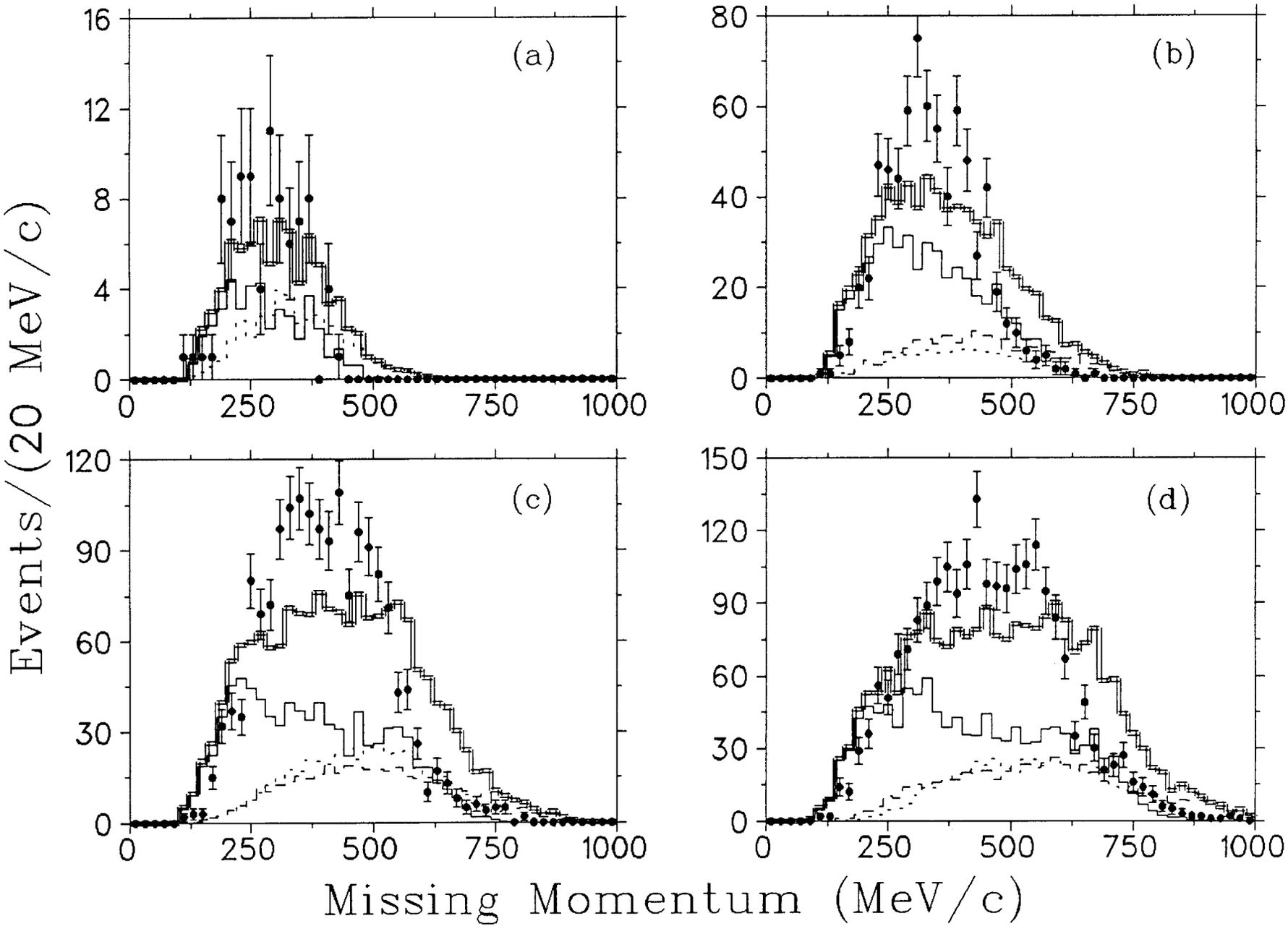

Fig. 7

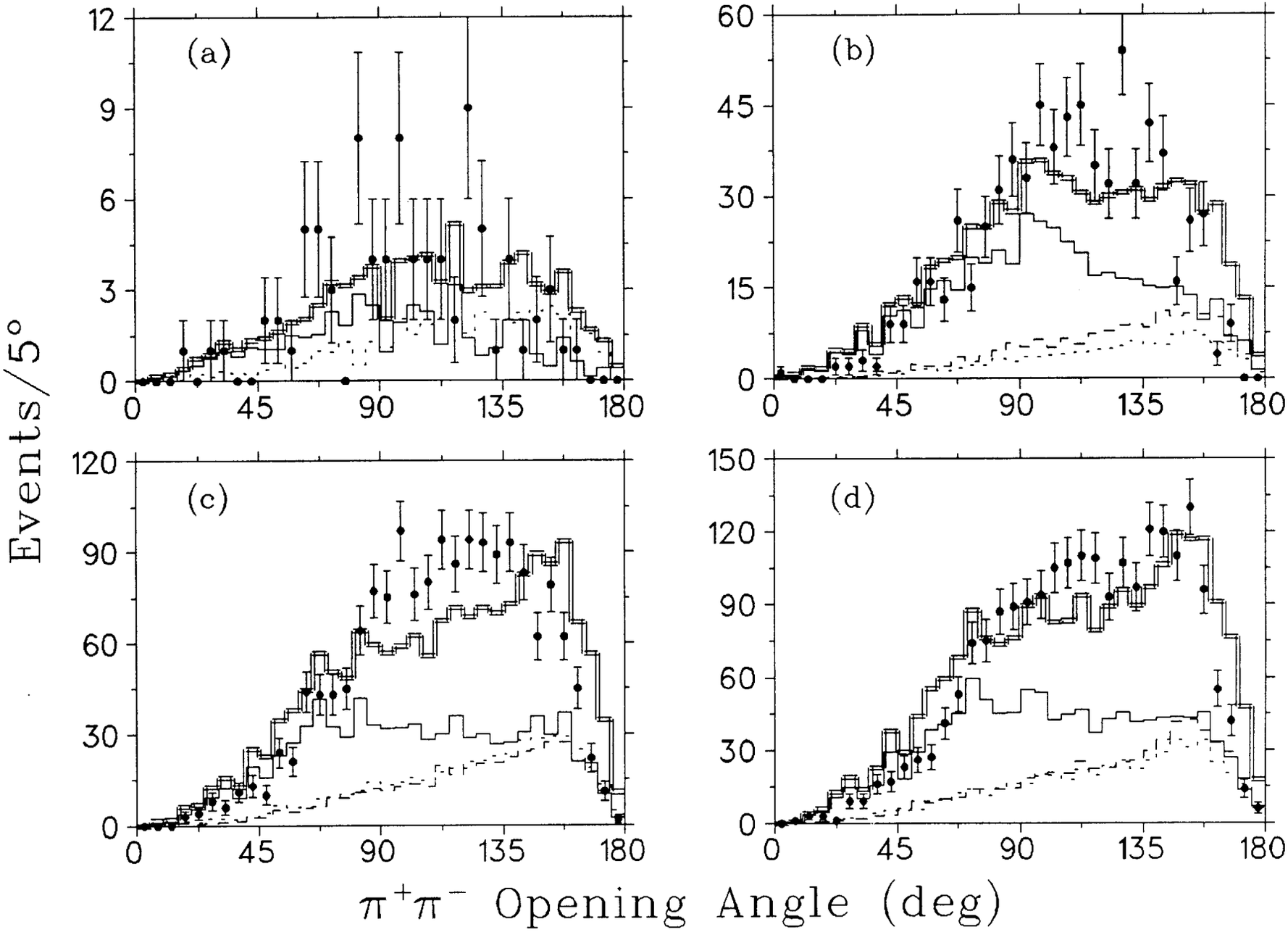

Fig. 8

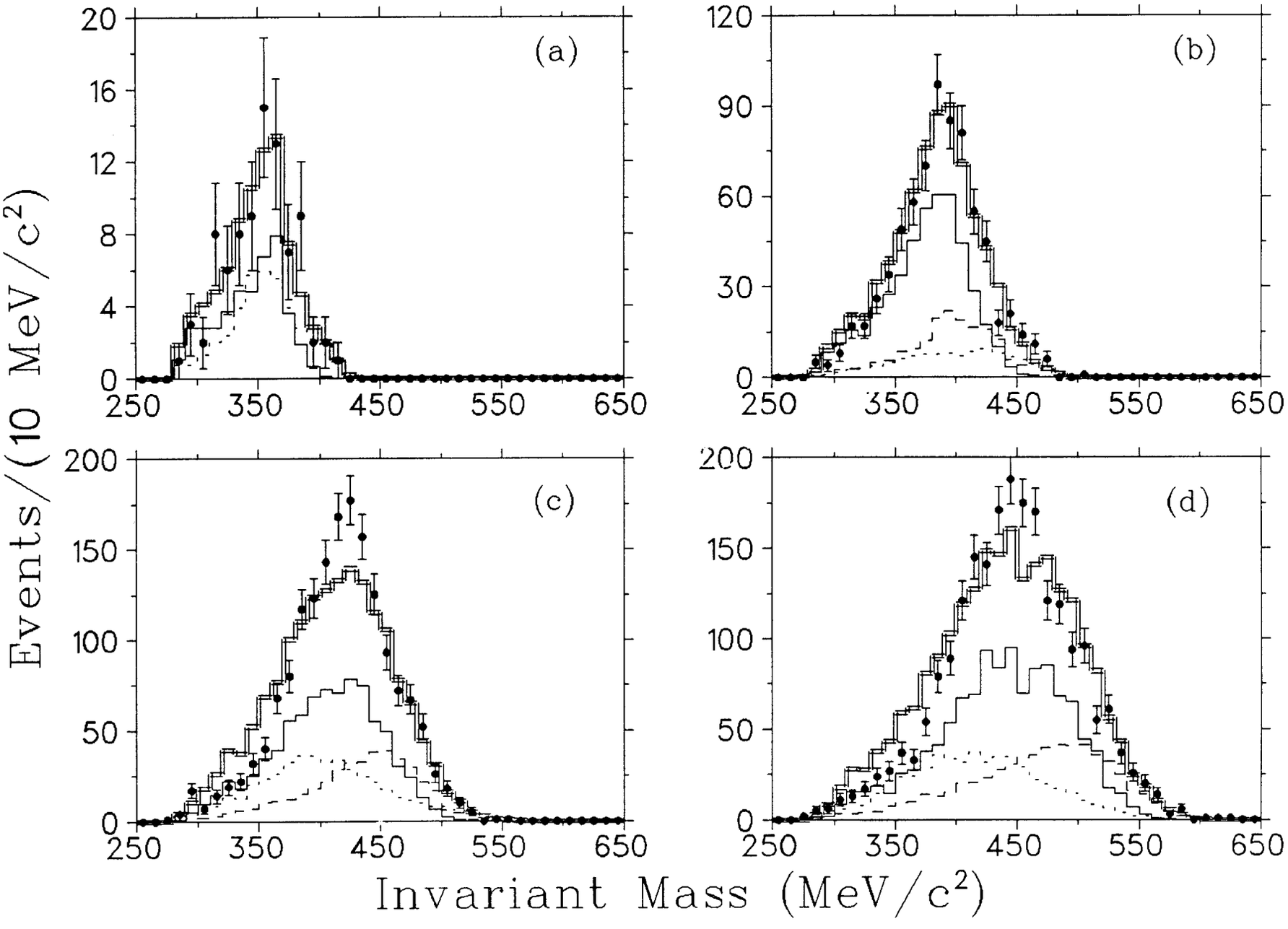
(a)
(b)
(c)
(d)
Events/(10 MeV/c²)
Invariant Mass (MeV/c²)
20
16
12
8
4
0
120
90
60
30
200
150
100
50
250
350
450
550
650

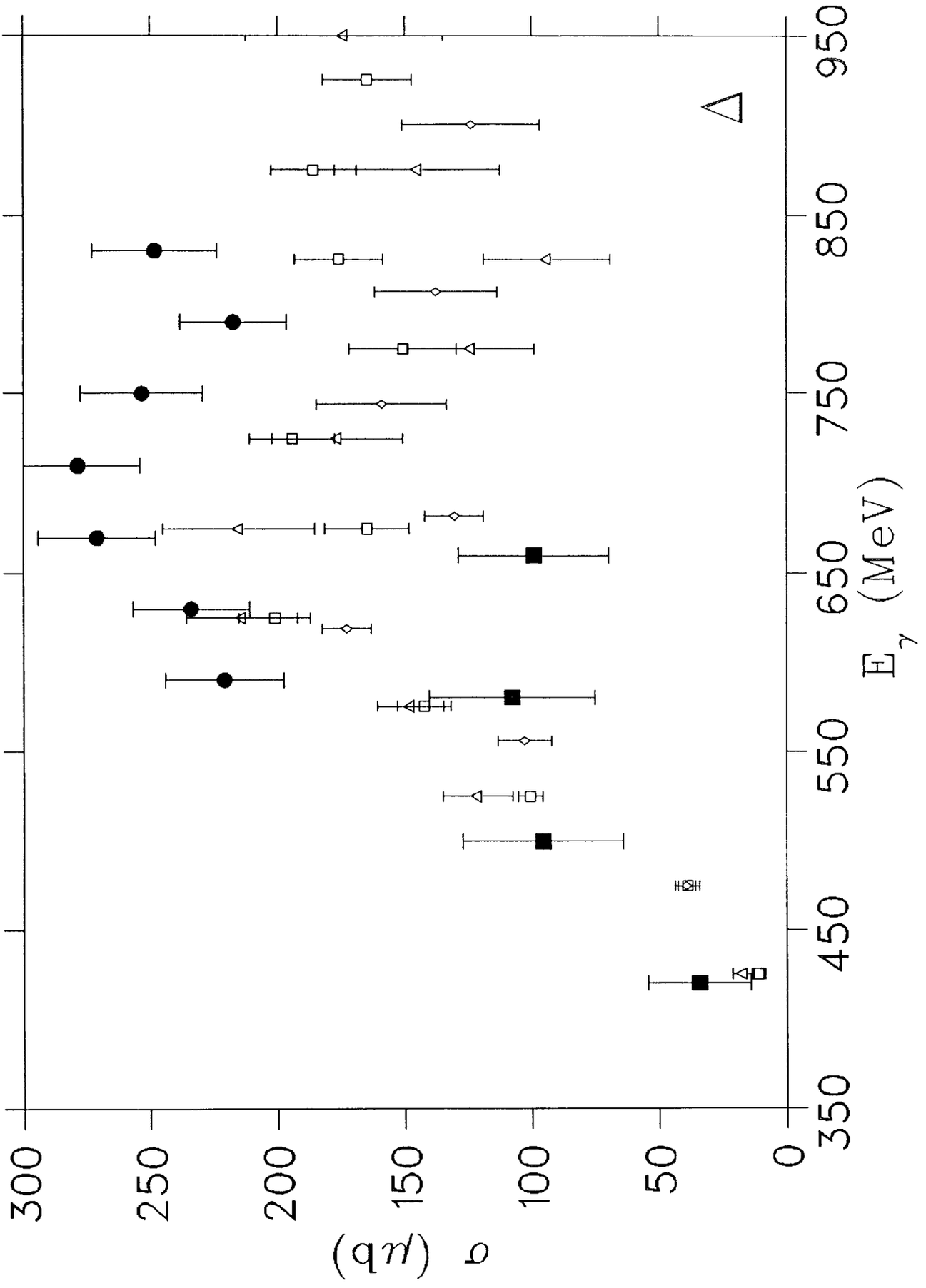
σ (μb)
300
250
200
150
100
50
0
350
450
550
650
750
850
950
E_γ (MeV)

Fig. 9

Fig. 1 0

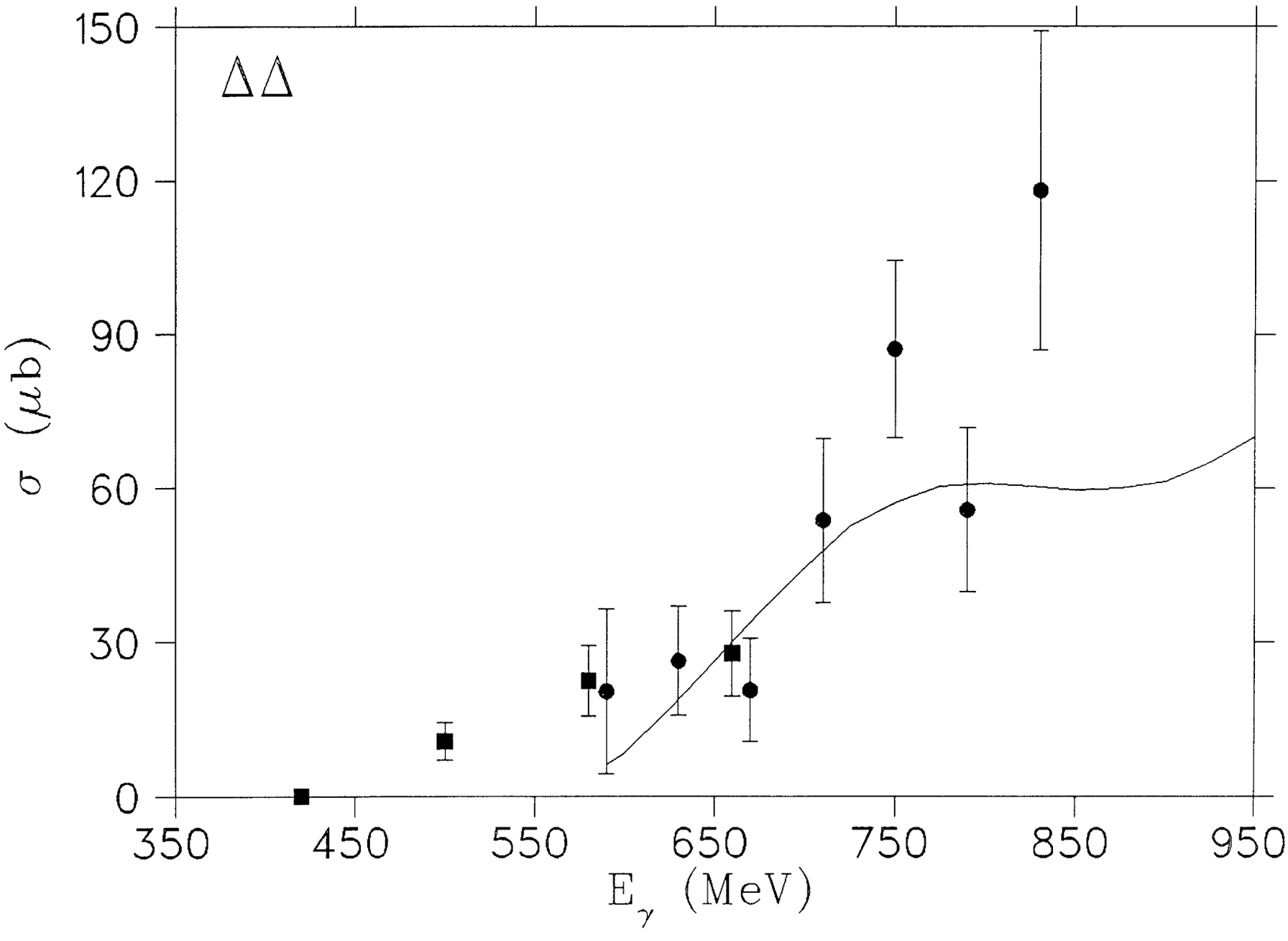

Fig. 1 1